

Post-aragonite phases of CaCO_3 at lower mantle pressures

Dean Smith,¹ Keith V. Lawler,² Austin W. Daykin,¹ Zachary Fussell,¹ G. Alexander Smith,² Christian Childs,¹ Jesse S. Smith,³ Chris J. Pickard,^{4,5} and Ashkan Salamat^{1,*}

¹*Department of Physics and Astronomy and HiPSEC,
University of Nevada Las Vegas, Las Vegas, Nevada 89154, USA*

²*Department of Chemistry and Biochemistry and HiPSEC,
University of Nevada Las Vegas, Las Vegas, Nevada 89154, USA*

³*High Pressure Collaborative Access Team, Geophysical Laboratory,
Carnegie Institution of Washington, Argonne, Illinois 60439, USA*

⁴*Department of Materials Science and Metallurgy,
University of Cambridge, Cambridge CB3 0FS, United Kingdom*

⁵*Advanced Institute for Materials Research, Tohoku University 2-1-1 Katahira, Aoba, Sendai 980-8577, Japan*
(Dated: June 21, 2019)

The stability, structure and properties of carbonate minerals at lower mantle conditions has significant impact on our understanding of the global carbon cycle and the composition of the interior of the Earth. In recent years, there has been significant interest in the behavior of carbonates at lower mantle conditions, specifically in their carbon hybridization, which has relevance for the storage of carbon within the deep mantle. Using high-pressure synchrotron X-ray diffraction in a diamond anvil cell coupled with direct laser heating of CaCO_3 using a CO_2 laser, we identify a crystalline phase of the material above 40 GPa – corresponding to a lower mantle depth of around 1,000 km – which has first been predicted by *ab initio* structure predictions. The observed sp^2 carbon hybridized species at 40 GPa is monoclinic with $P2_1/c$ symmetry and is stable up to 50 GPa, above which it transforms into a structure which cannot be indexed by existing known phases. We investigate with nudged elastic band (NEB) calculations the reaction mechanisms between relevant crystal phases of CaCO_3 and postulate that the mineral is capable of undergoing sp^2 - sp^3 hybridization change purely in the $P2_1/c$ structure – forgoing the accepted “post-aragonite” $Pm\bar{m}n$ structure.

INTRODUCTION

Carbonates play a significant role in the global carbon cycling through the subduction of carbonate-containing oceanic slab.[1, 2] Models dating back to the 1980s[3] notion that the majority of the Earth’s carbon is stored within the planet interior[4], either in some reduced form such as diamond or graphite, or as carbides at lower mantle and core conditions.[5, 6] Meanwhile, the existence of carbonate inclusions in “deep” diamonds suggest stability of the minerals under mantle pressures and temperatures.[7, 8] The stability and structures of carbonates at mantle conditions is thus important in order to further our understanding of numerous geological processes. While experiments designed to investigate such processes are often extremely challenging, the development of powerful evolutionary algorithms (for example USPEX [9]) and *ab initio* random structure searching (AIRSS [10, 11]) approaches allows for deeper insight into the structures available to these minerals at mantle conditions.

CaCO_3 transforms from its ambient pressure calcite-I ($R\bar{3}c$) to aragonite ($Pnma$) at comparatively low pressures,[12] and exhibits a large variety of calcite and calcite-like phases in the sub-10 GPa region [13–15] – some of which exhibit interesting chemistry at further compression.[16] The existence of phases beyond aragonite has been postulated since dynamic compression of aragonite CaCO_3 revealed discontinuities in its shock

Hugoniot at modest pressures.[17] However, static compression did not reveal a post-aragonite transition until more recently, when Santillan & Williams observed evidence of a new phase close to 50 GPa [18], which was attributed to an analogue of the trigonal post-witherite BaCO_3 . [19] Further study by Ono *et al.* dismisses the trigonal structure in favor of an orthorhombic one with space group $P2_12_12$. [20] Assignment of an orthorhombic post-aragonite phase was later supported by USPEX structural simulations, which suggested the $Pm\bar{m}n$ supergroup, and also predicted a further transformation into a *post*-post-aragonite $C222_1$ phase at megabar pressures.[21] Arapan *et al.* performed density functional theory (DFT) calculations on CaCO_3 and found good agreement with the $Pm\bar{m}n$ and $C222_1$ transition pressures predicted by Ref. 21.[22, 23] Evidence for *post*-post-aragonite had been observed experimentally and attributed to the pyroxene-type $C222_1$ structure,[24]. However, further structure searches using AIRSS predicts a CaCO_3 structure in the megabar regime with a difference – a $P2_1/c$ unit cell with pyroxene chains stacked out-of-phase, in contrast to the parallel chains in the $C222_1$ structure.[25] This difference reduces enthalpy significantly [25, 26] and is accompanied by a marked difference in Raman signature, which was used very recently by Lobanov *et al.* to confirm $P2_1/c$ -h as the stable structure for deep mantle CaCO_3 alongside X-ray diffraction.[27] Additionally, the AIRSS approach predicts a second monoclinic polymorph of CaCO_3 which

is stable at pressures equivalent to a depth of 1,000 km in the mantle, the $P2_1/c$ -l structure, which has remained unseen in compression experiments.

In a single-crystal X-ray diffraction study, Merlini *et al.* detect a triclinic $P\bar{1}$ structure (CaCO_3 -VI) above 15 GPa [28] which they attribute to the same transition detected, but not indexed, by previous dynamic compression experiments.[17] Interestingly, this triclinic phase had previously been predicted by the UPSEX code,[21] but dismissed by those authors as metastable with respect to $Pnma$ aragonite. This finding was echoed in Ref. 25, which found CaCO_3 -VI to be higher in enthalpy than aragonite and intrinsically strained, in spite of Ref. 28 measuring a higher density for CaCO_3 -VI than aragonite during their experiments. However, that CaCO_3 is able to occupy numerous metastable and transient phases at modest[13–16] and high[25, 28] pressures – much like its rich ground-state phase progression under compression – is a testament to its remarkably diverse polymorphism. We can attribute the richness of the CaCO_3 phase diagram to the close matching in size of the Ca^{2+} and CO_3^{2-} ions. Structural ramifications of the ionic size ratio in $M\text{CO}_3$ aragonite group crystals ($M = \text{Ca}, \text{Sr}, \text{Ba}, \text{Pb}$) is exemplified by observations made by Ref. 29, where combined high-resolution X-ray diffraction and neutron diffraction record an increasing degree of disorder in CO_3^{2-} units with decreasing cation size, with CaCO_3 having the largest variation in C-O bond lengths as well as a deviation from truly planar carbonate ions as a result of steric effects. Indeed, in the case of MgCO_3 , this ionic size effect inhibits the formation of an aragonite phase anywhere in its phase diagram and stabilises the $R\bar{3}c$ structure up to 85 GPa.[25] Similarly, for heavier carbonates where the sites occupied by CO_3^{2-} grow with M , we expect a comparatively simple phase evolution with pressure.

That the phase diagram of such a common and important mineral – and one exhibiting a wide array of stable structures which are relevant to geological processes in the Earth’s mantle – has only begun to be unraveled experimentally since the turn of the century[18, 20, 24, 27] is largely a result of experimental advances allowing powerful diagnostics such as X-ray diffraction to be performed *in situ* at combined high pressure and temperature.[30–33] Here, we present the addition of a transitional structure experimentally realized in CaCO_3 by utilizing a recently-developed instrument to allow *in situ* CO_2 laser annealing of minerals at high pressure – the $P2_1/c$ -l phase previously predicted by AIRSS calculations,[25] which exists as an intermediate between aragonite and “post-aragonite”.

STRUCTURE PREDICTIONS

We first revisit the *ab initio* random structure search (AIRSS) for CaCO_3 to 100 GPa in Ref. [25] by re-evaluating the initially reported structures and performing subsequent searches to uncover more candidate structures. Shown in Fig. 1, the enthalpy of the structures was computed by fully relaxing over a range of pressures with the Perdew-Burke-Ernzerhof for solids and surfaces (PBEsol) generalized gradient approximation (GGA)[34] density functional using the CASTEP[35] plane-wave DFT code. The choice of PBEsol as the density functional is taken as the calculations predict a calcite-I \rightarrow aragonite transition pressure of 1.4 GPa, which is closer to experimental observations (0.67 GPa, [12]) than the 4 GPa prediction attained when the Perdew-Burke-Ernzerhof (PBE) functional was used. The basis set cut-off energy was set to 700 eV using ultrasoft pseudopotentials with valence configurations of $3s^2 3p^6 4s^2$ for Ca, $2s^2 2p^2$ for C, and $2s^2 2p^4$ for O.[36] A Monkhorst-Pack[37] k -point grid with spacing $0.3\ 2\pi\ \text{\AA}^{-1}$ was used to sample the Brillouin zone. The results presented in Fig. 1 are in very good agreement with other DFT results.[22, 23, 26]

Beyond the stability field of $Pnma$ aragonite, we observe two competing monoclinic structures – the $P2_1/c$ -l structure from Ref. [25], which collapses into $P2_1/c$ -h at high pressures (dashed line in Fig. 1), as well as a second which we name $P2_1/c$ -ll. Interestingly, the $P2_1/c$ -ll phase which has comparably low enthalpy at low pressures to aragonite is not the previously known CaCO_3 (II) $P2_1/c$ structure.[13] $P2_1/c$ -l and $P2_1/c$ -ll are enthalpically competitive above 10 GPa, crossing one another in stability once at 18 GPa and once again at 37.5 GPa, whereupon the $P2_1/c$ -l remains the most stable until its collapse into $P2_1/c$ -h. The maximum separation of the two competing structures is 3.23 meV/formula unit (f.u.) ($0.074\ \text{kcal mol}^{-1}\ \text{f.u.}^{-1}$). Both the $P2_1/c$ -l and $P2_1/c$ -ll phases become more enthalpically more favorable than aragonite above 27.2 GPa. A further competitive phase is found in this region with $P2_12_12_1$ symmetry, and which eventually collapses into sp^3 -bonded $P2_12_12_1$ -h, however neither of these structures occupy the lowest enthalpy at any pressure. The previously reported $Pnma$ -h once again appears as a competitive phase, and is stable relative to aragonite and each of the aforementioned phases above 44 GPa, but at this point is not stable relative to $Pm\bar{m}n$. We observe a more narrow field of stability for $Pm\bar{m}n$ “post-aragonite” than our past study (42.4–58 here compared with 42–76 GPa in Ref. [25]) before $P2_1/c$ -h becomes the dominant phase until at least 100 GPa, as has recently been confirmed by experiments performed by Lobanov *et al.* in a diamond anvil cell with indirect laser heating.[27]

DFT computations for $P2_1/c$ -l CaCO_3 reveal a discontinuity in its enthalpy with pressure at around 7.5

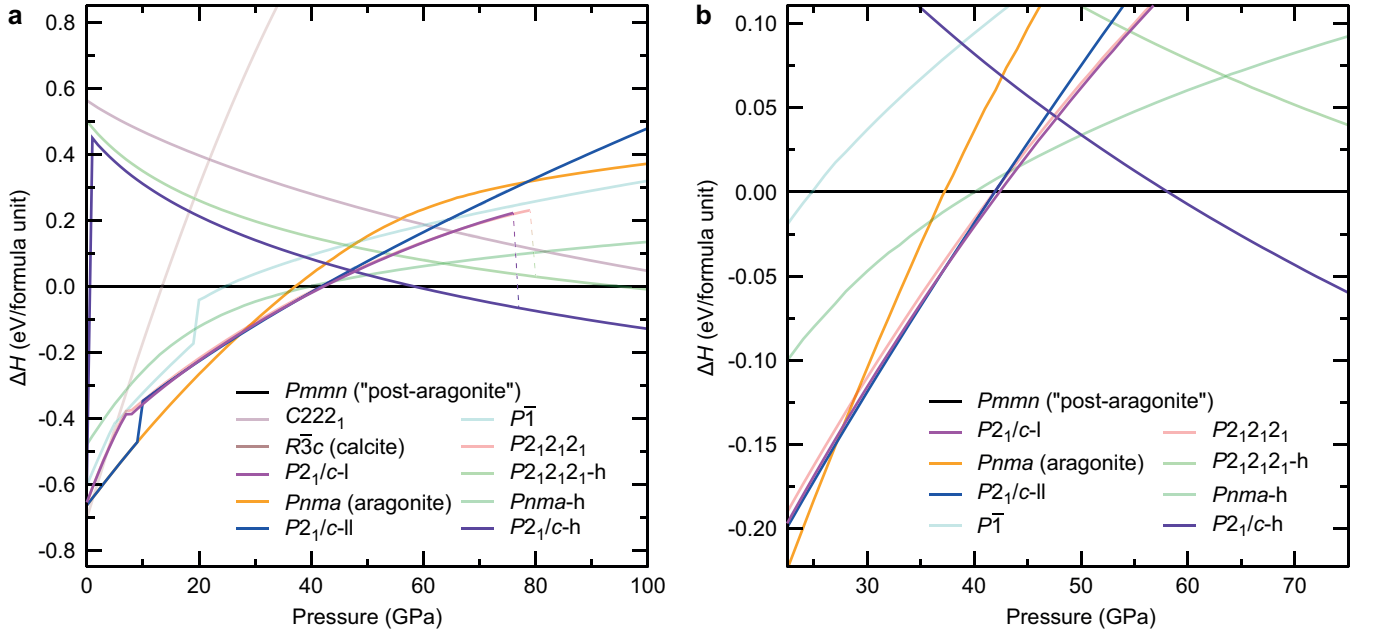


FIG. 1. Enthalpy per formula unit of CaCO_3 phases relative to "post-aragonite" $Pmmn$, ΔH , as a function of pressure (a) to 100 GPa, and (b) around the transitional post-aragonite region. Dashed lines indicate structures which collapse into high pressure phases. Pale lines indicate structures which are never thermodynamically stable.

GPa, which is reflected in the pressure-volume equation of state of the phase (Fig. 2a). As such behavior can be related to transitions, we investigate the structure and electronic structure of the $P2_1/c$ -I phase at low pressures. Fig. 2 shows the band structure and partial density of states (pDOS) of CaCO_3 in the $P2_1/c$ -I phase at ambient pressure and 10 GPa (Fig. 2b and c respectively). At ambient conditions, we see the signature of a resonant sp^2 CO_3^{2-} structure, s and p lobes which are near-symmetric (orange bands in Fig. 2b and c) and a valence composed of the remaining oxygen lone pairs tightly localized in energy close to the Fermi level (green bands). When pressure is increased to 10 GPa, the sp^2 features become smeared and more asymmetric, and are accompanied by additional curvature in the bands indicative of a changing bonding environment. Physically, this is accompanied by a puckering of CO_3^{2-} groups. The same is true for the oxygen lone pair features at the top of the valence band due to its splitting, as well as for the Ca p feature around -20 eV. These behaviors are suggestive of an interaction (such as polarization or charge transfer) at higher pressures between the Ca^{2+} and CO_3^{2-} species, and is supported further by the enhanced curvature of the conduction band at 10 GPa.

HIGH PRESSURE EXPERIMENTS

High pressure experiments were performed in diamond anvil cells (DACs) of custom design, equipped with conical-cut diamonds with a 70° opening and 300,

200 and 100 μm culets for three separate runs. Re foil with an initial thickness of 200 μm was pre-indented to form a gasket, and a 180, 120 and 60 μm hole were drilled, respectively, to serve as the sample chamber by laser micromachining.[38] CaCO_3 powder (Sigma-Aldrich ReagentPlus) was oven-dried and pressed into 10 μm -thick pellets. High pressure experiments typically have the requirement that samples are surrounded by some soft medium in order to serve as a quasi-hydrostatic pressure transmitter, and due to the high thermal conductivity of diamond, laser-heated DAC experiments require that samples are thermally isolated from the diamond anvils to achieve efficient and homogeneous heating.[32] Thus, CaCO_3 pellets were encased in either a medium of NaCl, KBr or Ar respectively, whose well-calibrated equation of state is also used to calculate pressure inside the sample chamber.

Laser heating was performed *in situ* at the ID-B diffraction beamline at HPCAT (Sector 16, Advanced Photon Source, Argonne IL) using the recently-developed instrument depicted in Figure 3. A Synrad *evolution*125 CO_2 laser operating at 10.6 μm was focused into the DAC to a spot size 35-80 μm . Thermal emission is collected using an achromatic objective shielded by a MgF_2 window to protect the glass optics from damage by the diffuse 10.6 μm radiation, and the image is then refocused onto a 50 μm pinhole made in a reflective surface. This pinhole acts as a spatial filter which samples a 7.5 μm region of the sample space, comparable to the X-ray spot size, and is aligned to the peak in the X-ray fluorescence such

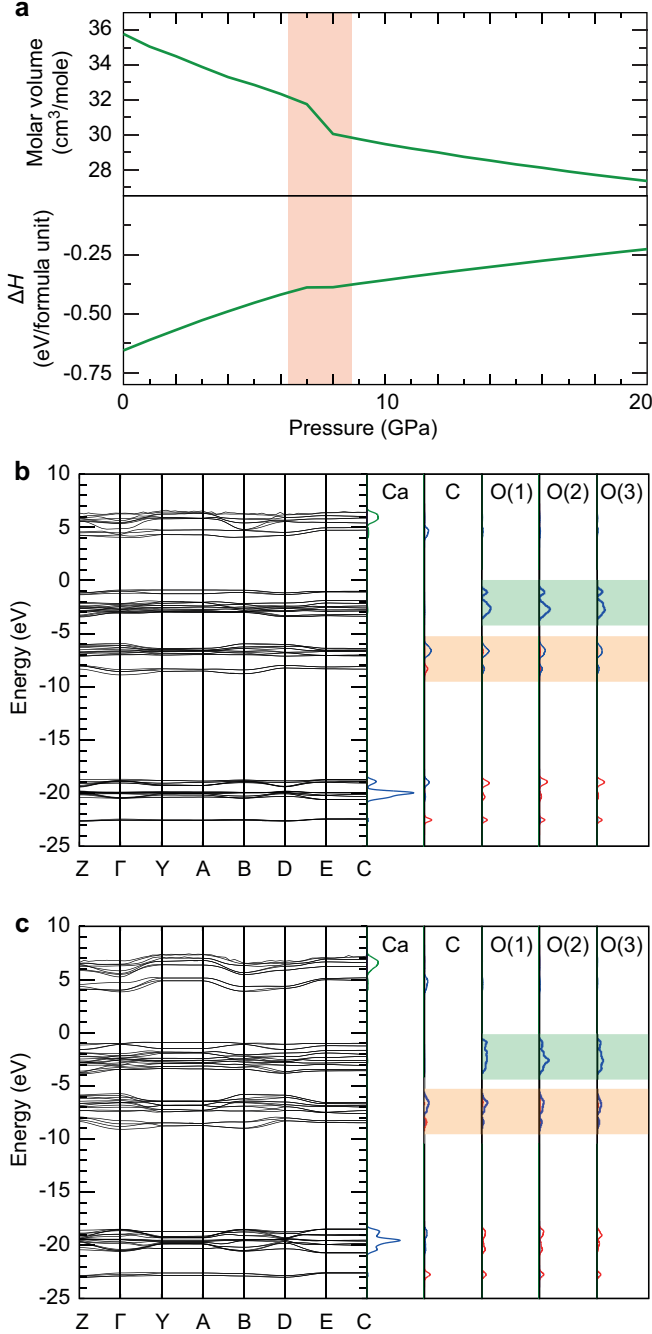


FIG. 2. Electronic evolution of $P2_1/c-1$ CaCO_3 to 20 GPa. (a) Relative enthalpy, ΔH , and volume display discontinuous behavior (relative to $Pmmn$ as in Fig. 1), (b,c) Calculated band structure (left) and partial density of states (right) at 0 and 10 GPa (pDOS due to s , p and d electrons are shown in red, blue and green respectively).

that temperature measurements are made from the precise location of X-ray diffraction. Reflected light from the pinhole surface is imaged onto a CCD camera for viewing the DAC interior during experiments.

For accurate alignment of the mid-IR laser spot to the

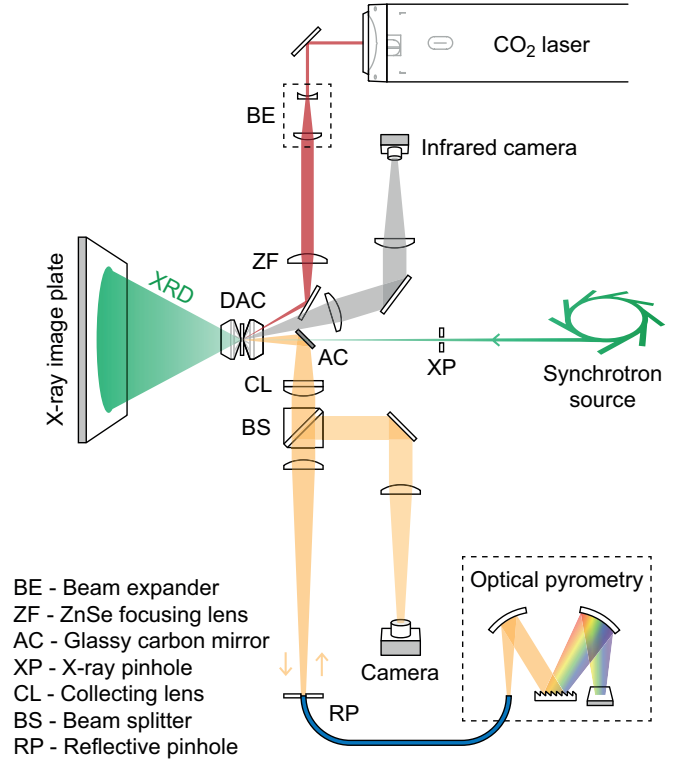


FIG. 3. *In situ* CO₂ laser heating system at the HPCAT ID-B diffraction beamline. Optical paths are shown for CO₂ laser delivery in red, pyrometry and visible spectrum visualization in yellow, mid-IR visualization in grey, and synchrotron X-ray diffraction in green.

X-ray and pyrometer focus, we employ a thermal imaging camera modified for microscopy (grey paths in Fig. 3). In this way, we are able to directly image the sample chamber in the 7–14 μm region prior to heating. This crucial development allows alignment of the laser spot to the sample area within the DAC using only milliwatts of laser power, whereas previous CO₂ laser heating instruments for DAC experiments have relied heavily on laser radiation coupling with material inside the sample chamber to create a thermal glow to allow the laser spot to be located, pre-heating the sample environment in some cases to in excess of 1,500 K. Implementation of mid-infrared microscopy to directly visualize the 10.6 μm laser spot makes it possible to avoid any pre-heating of the sample during the alignment procedure and before the formal beginning of an experiment.[39]

Angle-dispersive X-ray diffraction patterns were collected both during and after laser heating using monochromatic X-rays with $\lambda = 0.4066 \text{ \AA}$, with a Pilatus 1M detector.[40] The two-dimensional images were integrated into one-dimensional spectra using the *Dioptra* software package.[41] We gradually increased power density from the CO₂ laser as X-ray diffraction patterns were collected and observe for changes in the sample structure and texturing as a function of time and laser power.

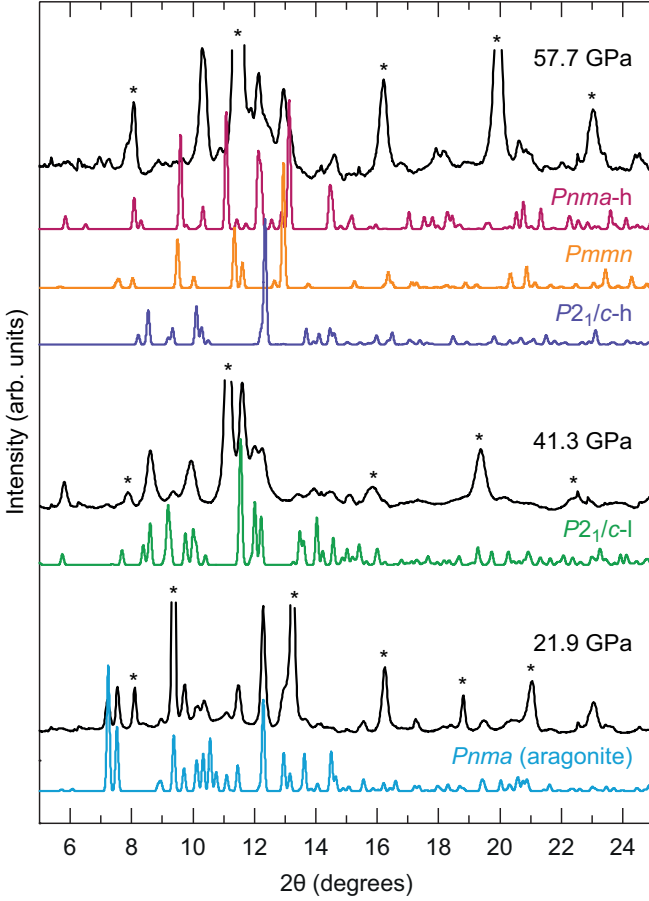


FIG. 4. Observed X-ray diffraction patterns at 21.9, 41.3 and 57.7 GPa following annealing with CO_2 laser (black plots), normalised to maximum intensity from CaCO_3 . Peaks marked with asterisks (*) are due to NaCl thermal insulator and pressure medium. Simulated diffraction patterns at $\lambda = 0.4066 \text{ \AA}$ and equivalent unit cell volumes for each phase are stacked beneath using computationally-generated structures. Annealed CaCO_3 data at 57.7 GPa is stacked against the three lowest enthalpy phases at this pressure and, notably, there is little similarity between the observed pattern and the “post-aragonite” $Pmmn$ phase, nor with other competitive structures.

Temperature determination by optical pyrometry when working with insulating materials such as carbonate minerals is complicated by their low emissivity in the visible, which remains low even into the mid-IR.[42, 43] The pyrometer is sufficiently sensitive to detect X-ray fluorescence from the sample and salt medium during diffraction collections, but does not detect any thermal emission from the CaCO_3 even when heating is performed at the highest power densities, making temperature estimation wrought with uncertainty. In Fig. 4, we show select data from the phase progression of CaCO_3 to 57.7 GPa, with laser annealing performed at roughly 5 GPa steps in pressure. Below 40 GPa, we observe only the expected Bragg reflections from aragonite.

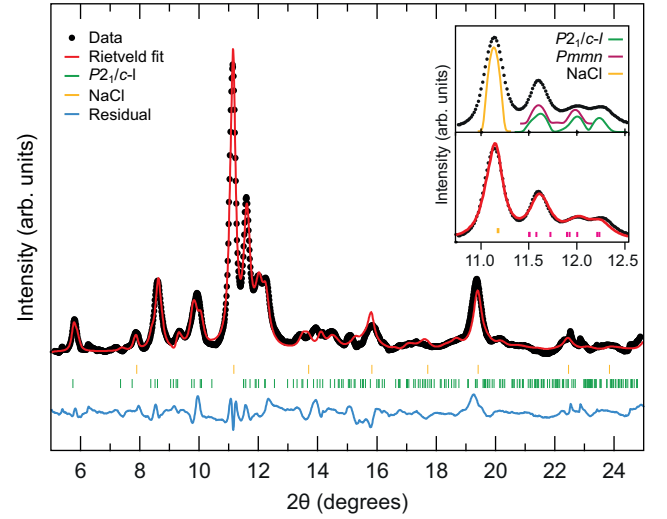


FIG. 5. Results of Rietveld structural refinement of X-ray diffraction pattern of CaCO_3 at (a) 41.3 GPa. A good fit ($wRp = 1.06\%$) is achieved using the $P2_1/c-l$ phase predicted by Ref. 25. (inset) Simulated X-ray diffraction patterns for $P2_1/c-l$ and $Pmmn$ structures compared with observed data (top) and Rietveld fit (bottom) to peaks in the 12° 2θ region using the $P2_1/c-l$ structure.

Although marginally lower in enthalpy than all competing phases between 27.2 GPa and 37.5 GPa, we did not observe the $P2_1/c-l$ structure when annealing at 30.6 or 36.2 GPa – further inspection into free energy arguments is sought to help understand this discrepancy. At 40 GPa, $P2_1/c-l$ exhibits the shortest Ca-Ca distance of any of the studied structures – 3.17 \AA vs. 3.47 in $Pnma$ aragonite and 3.65 in $P2_1/c-l$. This is a markedly compressed distance for two of the heaviest atoms in the cell, and it follows that this translates to a higher vibrational potential energy of any of the observed structures from a harmonic oscillator point-of-view. The zero point vibrational energy difference alone is likely large enough have the $P2_1/c-l$ phase energetically less favorable than $P2_1/c-l$, however a fuller evaluation of free energy from the quasi-harmonic approximation should show $P2_1/c-l$ as significantly higher in energy than Fig. 1 suggests.

At 41.3 GPa, a change in the diffraction pattern is observed, and the resulting pattern cannot be accounted for with the $Pnma$ aragonite or $Pmmn$ post-aragonite structures. We index the diffraction pattern at 41.3 GPa as corresponding to the monoclinic $P2_1/c-l$ structure, found by DFT calculations to be the most stable structure at 37.5–42.4 GPa (at 0 Kelvin). Fig. 5 shows the results of a Rietveld refinement of the crystal structure at 41.3 GPa using the GSAS software package with the $P2_1/c-l$ structure type as well as the high-pressure $Pm\bar{3}m$ structure of the NaCl thermal insulator. The full structural refinement on CaCO_3 has weighted R -factor value of 1.06% and a reduced χ^2 value of 4.202. This

crystal structure exhibits a strong peak at around 5.75° 2θ due to Bragg reflections from the (100) planes, which disappears beyond 50 GPa signifying a further transition. The inset of Fig. 5 shows the group of observed Bragg reflections around 12° 2θ alongside simulated patterns for the $P2_1/c$ -l and $Pm\bar{m}n$ phases (top panel), which show distinct differences in this region. The $Pm\bar{m}n$ "post-aragonite" structure (red) predicts two features between 11.5 - 12.0° , whereas the observed diffraction pattern contains three, which the $P2_1/c$ -l structure (green) is able to account for – further evidenced by the ability of this phase to accurately model the data in this region during Rietveld refinement (bottom panel). Table I shows our recorded experimental $P2_1/c$ -l structure from Rietveld refinement in which only the positions of the Ca atoms were refined and the $P2_1/c$ -l structure from simulation at equivalent pressures.

Above 50 GPa, there is a transition away from $P2_1/c$ -l. However, as is evident from the observed diffraction pattern in Fig. 4 and the simulated $Pm\bar{m}n$ diffraction pattern using appropriate lattice parameters (orange line in Fig. 4), the pattern above 50 GPa cannot be indexed with the "post-aragonite" phase. Upon reflection in the literature, the accepted $Pm\bar{m}n$ structure for post-aragonite CaCO_3 still remains to be subject to a rigorous structural refinement – both the original assignment of orthorhombic $P2_12_12$ by Ref. 20 and the following reassignment to $Pm\bar{m}n$ by Ref. 21 feature the same raw data and compare it with simulated patterns without performing any fitting procedure. Ref. 21 provides atomic positions for their experimental pattern, but there is no evidence for a structural refinement having been performed on the data. Until very recently, the raw data in Refs. 20 and 21 was the only published evidence of X-ray diffraction from $Pm\bar{m}n$ CaCO_3 , in spite of its recurrence in the literature.[22–24] Lobanov *et al.* have since heated CaCO_3 at 83 GPa using indirect laser-heating methods and published the raw diffraction pattern against simulated peaks. That the $Pm\bar{m}n$ phase is clearly not observed in our study warrants further investigation, and will be discussed in later sections.

It should also be noted that the metastable CaCO_3 -VI phase observed in Ref. [28] was not observed at any point during our high pressure experiment, in spite of their finding that it is higher in density than aragonite up to 40 GPa. The observation of metastable CaCO_3 phases by compression is not uncommon, very early diamond anvil cell high pressure studies uncovered the structure of CaCO_3 -II at 1.5 GPa.[13] Such metastable phases are likely avoided using our CO_2 laser annealing approach, since direct heating with $10.6 \mu\text{m}$ radiation allows uniform heating and homogeneous phase transformations at each density, allowing kinetic barriers that may lead to sluggish phase transitions and the development of metastable structures to be overcome with a high degree of control. Compared with alternative laser-

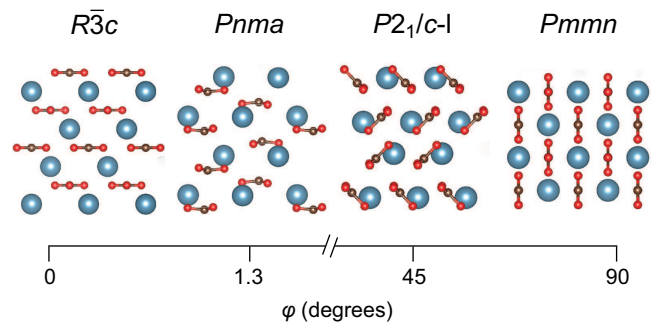


FIG. 6. Angle φ between CO_3^{2-} groups and Ca stacking in CaCO_3 crystal structures.

heating methods at high pressure, which employ a metallic coupling material to strongly absorb $\approx 1 \mu\text{m}$ radiation and indirectly heat the sample material, the CO_2 laser heating approach is a more close analogue of the geothermal annealing experienced by real mantle minerals. Future experiments could achieve highly accurate determination of ground state structures in minerals by combining the CO_2 laser annealing method employed here with the single crystal and multi-grain methodologies employed to solve more complex polymorphs such as the metastable CaCO_3 -VI, and while necessary preparations for such experiments are challenging even with near-IR laser irradiation[44], it is the most natural progression of high P,T experiments on geological materials to allow for the most accurate measurements. Indeed, even in the cases where such single crystals are not sustained to the most extreme pressures, the powder which emerges from single crystal breakdown across a first-order transition is of remarkably high quality compared with powdered samples pressed into pellets and can allow for full structural refinements.[45]

In Fig. 6, we show the ambient calcite ($R\bar{3}c$) and aragonite ($Pnma$) structures of CaCO_3 alongside the higher pressure "post-aragonite" ($Pm\bar{m}n$ [20]) and the $P2_1/c$ -l phase from this study, and follow the angle φ between CO_3^{2-} groups in each phase and their stacking plane in $R\bar{3}c$. In the ambient calcite and aragonite phases, a distinct ordering of the CO_3^{2-} units along these planes is evident. The CO_3^{2-} groups in aragonite are likely more ordered than is shown, since the aforementioned puckering of CO_3^{2-} units appears to exaggerate the apparent rotation with respect to the stacking plane. These co-planar groups are responsible for the anisotropic nature of a number of material properties in bulk CaCO_3 – for instance, the elastic constants of calcite vary by a factor of 4.5 across its crystallographic directions and the shear wave velocity by a factor of 1.5,[46] and natural CaCO_3 crystals famously exhibit strong birefringence and polarizing properties.[47] Co-planar CO_3^{2-} is present in the high-pressure CaCO_3 -II and CaCO_3 -III phases (C2

c axis [13] and $P2_1/c$ b axis [14] respectively, not shown), and in the $Pmmn$ post-aragonite phase. In the intermediate $P2_1/c$ -l phase, however, carbonate ions are at 45° to the $R\bar{3}c$ stacking plane and stack $AABB$ with one another. One could expect, then, that the physical properties of $P2_1/c$ CaCO_3 differ from those of calcite and aragonite, having a more isotropic elastic stiffness. Such crystallographic observations in deep Earth minerals can prove useful in advising geology and seismology, where mechanical properties of mantle constituents are directly recorded by sound velocities within the planet. That the carbonate ions occupy an intermediate angle in $P2_1/c$ -l CaCO_3 correlates with the structure occupying the energetic intermediate between aragonite and $Pmmn$, and that some intermediate featuring non-co-planar CO_3^{2-} is not surprising since in the absence of this intermediate phase, the carbonate ions in CaCO_3 would be required to undergo a near 90° rotation during the post-aragonite phase transition.

TRANSFORMATION MECHANISMS

To elucidate why the $P2_1/c$ -l phase has not previously been observed, and why it is realized only in a narrow pressure range, we carried out generalized solid-state nudged elastic band (g-SSNEB)[48] simulations at 20, 40, and 60 GPa along the reaction paths connecting both the $Pnma$ and $Pmmn$ phases to the $P2_1/c$ -l phase. The g-SSNEB pathways were calculated with a modified Vienna *ab initio* simulation package (VASP) version 5.4.1. The VASP calculations were set up similarly to the CASTEP calculations with the exceptions of the use of a Γ -centered k-point grid and the projector augmented wave (PAW)[49] method to describe the electron-ion interactions. The g-SSNEB calculations employed 24 images to connect the initial and final phases and allowed the atomic positions and lattice vectors of the images to vary. The gSSNEB simulations ran for at least 600 cycles or until the forces were below 10^{-2} eV/Å. The AIRSS predicted structures were re-optimized in VASP prior to g-SSNEB to minimize any inconsistencies between different DFT implementations.

The initial observation from Fig. 7 is that the defined phases maintained the same energy orderings as in Fig. 1, and that the transformation follows a similar trajectory at each pressure with variation in barrier heights and distances between the images. The transformation between $Pnma$ to $P2_1/c$ -l is marked by three processes: the rotation of the CO_3^{2-} groups, a shifting of the Ca^{2+} between atomic planes along the defined b -axis, and distortion of the unit cell to accommodate these motions. For reference, the $R\bar{3}c$ stacking planes are defined here as bc -planes perpendicular to the a -axis. The initial uphill steps from $Pnma$ have the system adopting a monoclinic cell angle. This provides an initial rotation of the CO_3^{2-}

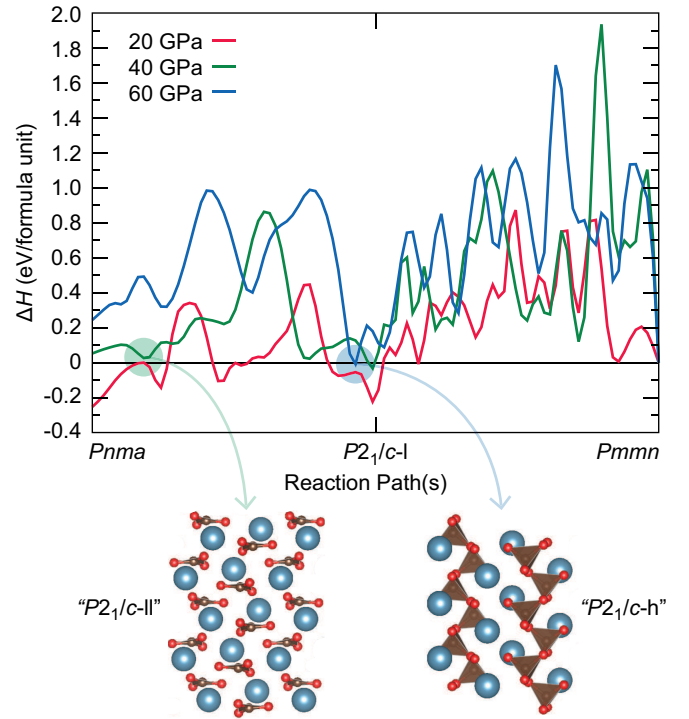


FIG. 7. Mechanism connecting the phases $Pnma \rightarrow P2_1/c$ -l $\rightarrow Pmmn$ at 20 (red), 40 (green), and 60 (blue) GPa with enthalpies relative to the $Pmmn$ phase. Distances along the pathway are taken as the Euclidean norm between the images normalized so the defined phases lie at unit values. Appearance of $P2_1/c$ -ll (green arrow) and $P2_1/c$ -h (blue arrow) structures along mechanism pathways are highlighted.

groups commensurate with the monoclinic angle causing the structure to resemble the $P2_1/c$ -ll phase. The first minima about 20% along the 40 GPa pathway very closely resembles the $P2_1/c$ -ll phase predicted by AIRSS (inset structure and green circle in Fig. 7), and it being slightly higher in enthalpy than $P2_1/c$ -l shows just how sensitive the magnitude of these small enthalpy changes are to the subtle differences in simulation set up. After the first barrier, the CO_3^{2-} then begin to rotate along a different axis and the cell angles return to nearly orthogonal. To accommodate this twisting of the CO_3^{2-} groups the Ca^{2+} switch stacking planes and migrate into a single ac -plane, until they become nearly planar at the minima halfway between $Pnma$ to $P2_1/c$ -l. The next uphill trajectory has the Ca^{2+} moving off of the single ac -plane while the box becomes more monoclinic, eventually reaching the global maximum along the pathway. This extrema has the largest unit cell volume of any of the structures, implying that the main enthalpic contribution is the PV work the system needs to apply against the external pressure source to accommodate that larger volume. Following that highest enthalpy barrier, the cell volume drops below the final unit cell volume, but the higher enthalpies relative to the $P2_1/c$ -l arise here from

the repulsive sterics of non-optimally positioned atoms, and the cell axis perpendicular to the stacking plane elongates to allow for longer Ca^{2+} distances.

The pathway connecting $P2_1/c$ -l to $Pm\bar{m}n$ is more complex with several peaks and valleys along the pathway. Here the peak enthalpies are mostly associated with the largest unit cell volume along the trajectory, again indicating that large cell volume distortions govern the energetics along the pathway. The $P2_1/c$ -l to $Pm\bar{m}n$ transformation appears to be more heavily marked by the movement of the Ca^{2+} . The trajectory begins with an increase in monoclinic angle followed by a return to a nearly orthorhombic box to accommodate a concerted counter-clockwise rotation of the Ca^{2+} when projected along the c -axis; which is completed by the very last peak/shoulder observed along each pathway followed by the reorganization of the atoms with respect to the $R\bar{3}c$ to reach the appropriate ABAB stacking scheme. After the first barrier and valley ($\sim 20\%$), what was the monoclinic angle shifts from being $> 90^\circ$ to being $< 90^\circ$ tilting the unit cell in the opposite direction. This tilt becomes quite pronounced until returning to nearly orthorhombic at the first large barrier around 40% of the way through the pathway. After the first major energy barrier, half of the CO_3^{2-} groups are oriented in the same fashion of as in $Pm\bar{m}n$, but the other half still require a nearly 90° rotation. The latter part of the pathway is defined by an undulating cell tilt to allow the other CO_3^{2-} groups to rotate into their correct positioning for $Pm\bar{m}n$. At all pressures there does not appear to be any shift away from sp^2 bonding in the CO_3^{2-} , indicating that electrostatic repulsion and PV work are the dominating factors in the increased enthalpy of the systems.

The maximum barrier heights along the $Pnma$ to $P2_1/c$ -l pathway are 0.14, 0.16, and 0.15 eV/atom for 20, 40 and 60 GPa, respectively. These correspond to a thermal energy ($\Delta H/atom = \frac{3}{2}kT$) of 1060, 1250, and 1150 K for 20, 40 and 60 GPa, respectively. Favorable entropic effects for the more disordered intermediates should lower these temperatures, but not significantly. While $P2_1/c$ -l is the most enthalpically favorable structure at 40 GPa, there is the clear necessity for the system to be driven to a temperature $\sim 1000^\circ\text{C}$ in order to overcome the kinetic barrier into the $P2_1/c$ -l phase – reinforcing the necessity of CO_2 laser annealing for investigating the phase progression in this and in other other geologically-relevant systems. A cold compression will not observe the $P2_1/c$ -l phase, and that the phase has not yet been observed in over a decade of post-aragonite CaCO_3 experiments demonstrates that only an appropriately-designed experiment can unveil the true phase progression of mantle minerals.

Meanwhile, the maximum barrier heights along the $P2_1/c$ -l to $Pm\bar{m}n$ pathway are 0.22, 0.39, 0.30 eV/atom at 20, 40 and 60 GPa respectively – corresponding to 1730, 3030, and 2350 K respectively. These barriers are

much larger than those along the $Pnma$ to $P2_1/c$ -l pathway and are more predominant at higher pressure. These predicted barriers should be considered as upper bounds to the actual energetic barrier since NEB is by no means exhaustive of all possible transition pathways and other free energy concerns may alter those values. With that being said, if those high barriers are in fact the case, then question must be begged of how the enthalpically favorable $Pm\bar{m}n$ phase can be reached at pressures from 50-80 GPa, *i.e.* 1250-1850 km within the mantle and 2000-2200 K?[50]. We made preliminary attempts to determine alternate pathways directly connecting the $Pnma$ to $Pm\bar{m}n$ phase, however, each featured barriers at least 2.5 times those between $P2_1/c$ -l and $Pm\bar{m}n$. The reason for this is the concerted rotation of the CO_3^{2-} and re-arrangement of Ca^{2+} groups necessitates that several groups come very close to one another in the middle of the cell, even leaving atoms directly on top of one another in the original images. This leads to very high repulsion energies making those pathways unfavorable, and indicating that some other intermediate phase must connect the $Pnma$ and $Pm\bar{m}n$ phases if the $Pm\bar{m}n$ phase can be achieved at all.

Along the 60 GPa $Pnma$ to $P2_1/c$ -l reaction path, an intermediate structure actually becomes marginally more enthalpically favorable than the $P2_1/c$ -l phase. This structure corresponds to a lower symmetry, triclinic version of the sp^3 bonded $P2_1/c$ -h phase (inset structure in Fig. 7). At the point along the pathway at 60 GPa emphasized with the blue circle in Fig. 7, the counter-rotated CO_3^{2-} groups become sufficiently close that they react and bond to form the pyroxene-like chains of CO_4 sp^3 tetrahedra. The raise in enthalpy at the very end of the 60 GPa $Pnma$ to $P2_1/c$ -l pathway comes from breaking a C-O bond to return to the sp^2 bound CO_3^{2-} groups. The ability at higher pressures to form $P2_1/c$ -h before $P2_1/c$ -l short circuits the mechanistic pathway we have illustrated, and allows for a lower energy pathway connecting the triclinic $P2_1/c$ -h rather than $Pm\bar{m}n$. Re-optimizations indicate that the triclinic $P2_1/c$ -h structure becomes more enthalpically favorable by 50 GPa, precisely when the $P2_1/c$ -l is no longer observed experimentally.

These complicated kinetics alongside our observation of experimental X-ray diffraction patterns which are not consistent with the reported $Pm\bar{m}n$ casts some doubt over the claims made in recent years that aragonite will transform into a "post-aragonite" with $Pm\bar{m}n$ symmetry. This doubt is further reinforced by the aforementioned lack of published structural refinements on the now-accepted structure. Furthermore, Ref. [27] reveals a marked distinction in quality of diffraction data between their reported $Pm\bar{m}n$ and $P2_1/c$ -h samples, strongly evidenced by their ability to perform a Le Bail refinement on $P2_1/c$ -h at 105 GPa, but reporting only a qualitative comparison between data at 83 GPa and a simu-

TABLE I. Crystallographic parameters of $P2_1/c$ -l CaCO_3 from experiment and DFT.

	Pressure	Space group	Lattice parameters			Species	Atomic coordinates		
	(GPa)		(Å, deg.)				x	y	z
Experiment	41.3	$P2_1/c$	$a = 4.85656$	$b = 3.34107$	$c = 12.09737$	Ca	0.08584	-0.19861	0.40372
			$\alpha = 90.0$	$\beta = 123.3300$	$\gamma = 90.0$	C	-0.53927	-0.05723	0.13886
						O(1)	0.27374	-0.19485	0.17202
						O(2)	-0.24458	-0.18693	0.18103
						O(3)	-0.66300	-0.78832	0.04896
Simulation	40	$P2_1/c$	$a = 4.71660$	$b = 3.34070$	$c = 12.42170$	Ca	0.09381	-0.18682	0.39673
			$\alpha = 90.0$	$\beta = 123.2500$	$\gamma = 90.0$	C	-0.53927	-0.05723	0.13886
						O(1)	0.27374	-0.19485	0.17202
						O(2)	-0.24458	-0.18693	0.18103
						O(3)	-0.66300	-0.78832	0.04896

lated $Pm\bar{m}n$ pattern – *i.e.* experimental evidence for the existence of the $Pm\bar{m}n$ structure is not as strong as evidence for each of the $P2_1/c$ structures. With this in mind and with support from mechanistic calculations reported here showing the arrival of a structure above 50 GPa which is identical to $P2_1/c$ -h, we postulate that – in spite of its enthalpic favorability (Fig. 1) – $Pm\bar{m}n$ may not be a real structure of CaCO_3 at mantle conditions. Tentative analysis of the post- $P2_1/c$ -l data shown in Fig. 4 suggests that some mixture of the $P2_1/c$ -l and -h may exist over some pressure range over which CaCO_3 is undergoing an isosymmetric transition.

CONCLUSIONS

We report an additional polymorph of CaCO_3 – $P2_1/c$ -l – which is stable at pressures equivalent to a mantle depth around 1,000 km, first predicted to be stable by *ab initio* random structure searching [25] and now realized by utilizing direct annealing of the mineral with 10.6 μm radiation from a CO_2 laser with *in situ* X-ray diffraction. Above 50 GPa, the $P2_1/c$ -l phase transforms into a structure which cannot be indexed as the formally accepted “post-aragonite”. Investigation of the reaction pathways between $P2_1/c$ -l and $Pm\bar{m}n$ “post-aragonite” sees a rising kinetic barrier with increasing pressure,

slightly exceeding the temperatures estimated at equivalent depths inside the mantle by the PREM model,[50] which may suggest an absence of $Pm\bar{m}n$ CaCO_3 in the Earth’s interior. Further work is required to formally investigate the phase progression of $P2_1$ – c -l CaCO_3 upon further compression, but AIRSS and g-SSNEB calculations tentatively suggest that an isosymmetric transition from $P2_1/c$ -l to $P2_1/c$ -h may be able to facilitate direct sp^2 - sp^3 conversion within mantle carbonates.

This research was sponsored in part by the National Nuclear Security Administration under the Stewardship Science Academic Alliances program through DOE Cooperative Agreement #DE-NA0001982. Portions of this work were performed at HPCAT (Sector 16), Advanced Photon Source (APS), Argonne National Laboratory. HPCAT operations are supported by DOE-NNSA under Award No. DE-NA0001974 and DOE-BES under Award No. DE-FG02-99ER45775, with partial instrumentation funding by NSF. APS is supported by DOE-BES, under Contract No. DE-AC02-06CH11357. C.J.P. acknowledges financial support from the Engineering and Physical Sciences Research Council (EPSRC) of the UK under Grant No. EP/P022596/1. C.J.P. is also supported by the Royal Society through a Royal Society Wolfson Research Merit Award.

* Author to whom correspondence should be addressed: salamat@physics.unlv.edu

- [1] A. R. Thomson, M. J. Walter, S. C. Kohn, and R. A. Brooker, *Nature* **529**, 76 (2016).
- [2] S. Huang, J. Farka, and S. B. Jacobsen, *Geochim. Cosmochim. Acta* **75**, 4987 (2011).

- [3] B. Marty and A. Jambon, *Earth Planet. Sci. Lett.* **83**, 16 (1987).
- [4] R. Dasgupta and M. M. Hirschmann, *Earth Planet. Sci. Lett.* **298**, 1 (2010).
- [5] L. Gao, B. Chen, J. Wang, E. E. Alp, J. Zhao, M. Lerche, W. Sturhahn, H. P. Scott, F. Huang, Y. Ding, S. V. Sino-geikin, C. C. Lundstrom, J. D. Bass, and J. Li, *Geophys. Res. Lett.* **35**, L17306 (2008), l17306.
- [6] G. Fiquet, J. Badro, E. Gregoryanz, Y. Fei, and F. Occelli, *Phys. Earth Planet. Inter.* **172**, 125 (2009).

- [7] F. E. Brenker, C. Vollmer, L. Vincze, B. Vekemans, A. Szymanski, K. Janssens, I. Szaloki, L. Nasdala, W. Joswig, and F. Kaminsky, *Earth Planet. Sci. Lett.* **260**, 1 (2007).
- [8] F. V. Kaminsky, R. Wirth, and A. Schreiber, *Can. Mineral.* **51**, 669 (2013).
- [9] C. W. Glass, A. R. Oganov, and N. Hansen, *Comput. Phys. Commun.* **175**, 713 (2006).
- [10] C. J. Pickard and R. J. Needs, *Phys. Rev. Lett.* **97**, 045504 (2006).
- [11] C. J. Pickard and R. J. Needs, *J. Phys.: Condens. Matter* **23**, 053201 (2011).
- [12] C. Biellmann, F. Guyot, P. Gillet, and B. Reynard, *Eur. J. Mineral.* **5**, 503 (1993).
- [13] L. Merrill and W. A. Bassett, *Acta Crystall. B - Stru.* **31**, 343 (1975).
- [14] J. R. Smyth and T. J. Ahrens, *Geophys. Res. Lett.* **24**, 1595 (1997).
- [15] N. Ishizawa, H. Setoguchi, and K. Yanagisawa, *Sci. Rep.* **3** (2013), 10.1038/srep02832.
- [16] K. Catalli, *Am. Mineral.* **90**, 1679 (2005).
- [17] J. Vizgirda and T. J. Ahrens, *J. Geophys. Res.: Sol. Ea.* **87**, 4747 (1982).
- [18] J. Santillán and Q. Williams, *Am. Mineral.* **89**, 1348 (2004).
- [19] C. M. Holl, J. R. Smyth, H. M. S. Laustsen, S. D. Jacobsen, and R. T. Downs, *Phys. Chem. Miner.* **27**, 467 (2000).
- [20] S. Ono, T. Kikegawa, Y. Ohishi, and J. Tsuchiya, *Am. Mineral.* **90**, 667 (2005).
- [21] A. R. Oganov, C. W. Glass, and S. Ono, *Earth Planet. Sci. Lett.* **241**, 95 (2006).
- [22] S. Arapan, J. S. de Almeida, and R. Ahuja, *Phys. Rev. Lett.* **98**, 268501 (2007).
- [23] S. Arapan and R. Ahuja, *Phys. Rev. B* **82**, 184115 (2010).
- [24] S. Ono, T. Kikegawa, and Y. Ohishi, *Am. Mineral.* **92**, 1246 (2007).
- [25] C. J. Pickard and R. J. Needs, *Phys. Rev. B* **91**, 104101 (2015).
- [26] X. Yao, C. Xie, X. Dong, A. R. Oganov, and Q. Zeng, *arXiv:1707.03226v1*.
- [27] S. S. Lobanov, X. Dong, N. S. Martirosyan, A. I. Samtsevich, V. Stevanovic, P. N. Gavryushkin, K. D. Litasov, E. Greenberg, V. B. Prakapenka, A. R. Oganov, and A. F. Goncharov, *Phys. Rev. B* **96**, 104101 (2017).
- [28] M. Merlini, M. Hanfland, and W. Crichton, *Earth Planet. Sci. Lett.* **333-334**, 265 (2012).
- [29] S. M. Antao and I. Hassan, *Can. Mineral.* **47**, 1245 (2009).
- [30] V. B. Prakapenka, A. Kubo, A. Kuznetsov, A. Laskin, O. Shkurikhin, P. Dera, M. L. Rivers, and S. R. Sutton, *High Pressure Res.* **28**, 225 (2008).
- [31] A. Salamat, R. A. Fischer, R. Briggs, M. I. McMahon, and S. Petitgirard, *Coord. Chem. Rev.* **277-278**, 15 (2014).
- [32] S. Petitgirard, A. Salamat, P. Beck, G. Weck, and P. Bouvier, *J. Synchrotron Rad.* **21**, 89 (2014).
- [33] Y. Meng, R. Hrubiak, E. Rod, R. Boehler, and G. Shen, *Rev. Sci. Instrum.* **86**, 072201 (2015).
- [34] J. P. Perdew, A. Ruzsinszky, G. I. Csonka, O. A. Vydrov, G. E. Scuseria, L. A. Constantin, X. Zhou, and K. Burke, *Phys. Rev. Lett.* **100**, 136406 (2008).
- [35] S. J. Clark, M. D. Segall, C. J. Pickard, P. J. Hasnip, M. I. J. Probert, K. Refson, and M. C. Payne, *Z. Kristallogr. - Cryst. Mater.* **220**, 567 (2009).
- [36] D. Vanderbilt, *Phys. Rev. B* **41**, 7892 (1990).
- [37] H. J. Monkhorst and J. D. Pack, *Phys. Rev. B* **13**, 5188 (1976).
- [38] R. Hrubiak, S. Sinogeikin, E. Rod, and G. Shen, *Rev. Sci. Instrum.* **86**, 072202 (2015).
- [39] Manuscript in preparation.
- [40] C. Broennimann, E. F. Eikenberry, B. Henrich, R. Horisberger, G. Huelsen, E. Pohl, B. Schmitt, C. Schulze-Bries, M. Suzuki, T. Tomizaki, H. Toyokawa, and A. Wagner, *J. Synchrotron Radiat.* **13**, 120 (2006).
- [41] C. Prescher and V. B. Prakapenka, *High Pressure Res.* **35**, 223 (2015).
- [42] M. D. Lane, *J. Geophys. Res.: Planet.* **104**, 14099 (1999).
- [43] T. D. Glotch and A. D. Rogers, *J. Geophys. Res.: Planet.* **118**, 126 (2013).
- [44] M. Merlini, M. Hanfland, A. Salamat, S. Petitgirard, and H. Müller, *Am. Mineral.* **100**, 2001 (2015).
- [45] F. Datchi, B. Mallick, A. Salamat, and S. Ninet, *Phys. Rev. Lett.* **108**, 125701 (2012).
- [46] C.-C. Chen, C.-C. Lin, L.-G. Liu, S. V. Sinogeikin, and J. D. Bass, *Am. Mineral.* **86**, 1525 (2001).
- [47] G. Ropars, G. Gorre, A. L. Floch, J. Enoch, and V. Lakshminarayanan, *P. Roy. Soc. A - Math. Phys.* **468**, 671 (2011).
- [48] D. Sheppard, P. Xiao, W. Chemelewski, D. D. Johnson, and G. Henkelman, *J. Chem. Phys.* **136**, 074103 (2012).
- [49] P. E. Blöchl, *Phys. Rev. B* **50**, 17953 (1994).
- [50] A. M. Dziewonski and D. L. Anderson, *Phys. Earth Planet. Inter.* **25**, 297 (1981).